# Epidermal Growth Factor Receptor Targeted Nuclear Delivery and High-Resolution Whole Cell X-ray Imaging of Fe$_3$O$_4$@TiO$_2$ Nanoparticles in Cancer Cells

Ye Yuan,[†] Si Chen,[‡] Tatjana Paunesku,[†] Sophie Charlotte Gleber,[‡] William C. Liu,[†] Caroline B. Doty,[†] Rachel Mak,[§] Junjing Deng,[§] Qiaoling Jin,[‡] Barry Lai,[‡] Keith Brister,[⊥] Claus Flachenecker,[∥] Chris Jacobsen,[‡,§] Stefan Vogt,[‡] and Gayle E. Woloschak[†,*]

[†]Department of Radiation Oncology, Northwestern University, Chicago, Illinois 60611, United States, [‡]X-ray Science Division, Argonne National Laboratory, Argonne, Illinois 60439, United States, [§]Department of Physics and Astronomy, Northwestern University, Evanston, Illinois 60208, United States, [⊥]Northwestern Synchrotron Research Center, Argonne, Illinois 60439, United States, and [∥]Carl Zeiss X-ray Microscopy, Pleasanton, California 94588, United States

ABSTRACT Sequestration within the cytoplasm often limits the efficacy of therapeutic nanoparticles that have specific subcellular targets. To allow for both cellular and subcellular nanoparticle delivery, we have created epidermal growth factor receptor (EGFR)-targeted Fe$_3$O$_4$@TiO$_2$ nanoparticles that use the native intracellular trafficking of EGFR to improve internalization and nuclear transloca-tion in EGFR-expressing HeLa cells. While bound to EGFR, these nanoparticles do not interfere with the interaction between EGFR and karyopherin-β, a protein that is critical for the translocation of
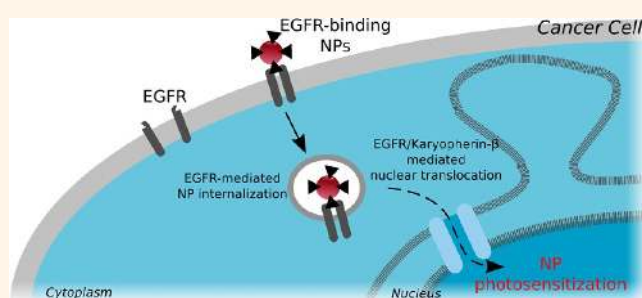
ligand-bound EGFR to the nucleus. Thus, a portion of the EGFR-targeted nanoparticles taken up by the cells also reaches cell nuclei. We were able to track nanoparticle accumulation in cells by flow cytometry and nanoparticle subcellular distribution by confocal fluorescent microscopy indirectly, using fluorescently labeled nanoparticles. More importantly, we imaged and quantified intracellular nanoparticles directly, by their elemental signatures, using X-ray fluorescence microscopy at the Bionanoprobe, the first instrument of its kind in the world. The Bionanoprobe can focus hard X-rays down to a 30 nm spot size to map the positions of chemical elements tomographically within whole frozen-hydrated cells. Finally, we show that photoactivation of targeted nanoparticles in cell nuclei, dependent on successful EGFR nuclear accumulation, induces significantly more double-stranded DNA breaks than photoactivation of nanoparticles that remain exclusively in the cytoplasm.

KEYWORDS: nanoparticles · titanium dioxide · photoactivation · X-ray fluorescence microscopy · epidermal growth factor receptor

Different approaches for the targeted delivery of nanoparticles (NPs) have been devised; nevertheless very often once inside cells NPs are unable to leave endocytic vesicles and end up in lysosomes or removed from cells by exocytosis.[1,2] Ideally, the targeting of NPs should not end with cell delivery, but with placement of NPs in the subcellular compartment, where their pre-sence is desired. For DNA-cleaving NPs, made of photoactivatable materials such as TiO$_2$,[3−5] the cell nucleus is strategically the best sub-cellular target. An optimal vehicle for such delivery could be the epidermal growth factor receptor (EGFR). This cell membrane receptor is overexpressed in many cancers.[6−13] EGFR and its ligand, epidermal growth factor (EGF), can be found in cell nuclei.[14−18] Nuclear accumulation of EGFR plays many roles in cells; this accumulation is especially pro-nounced in highly proliferative tissues and cancer cells.[13,19−24] The transport of EGFR into the nucleus can be triggered either by binding of natural ligands or, in the ab-sence of ligands, by exposure to stress such as irradiation.[23,25,26] Internalization of the

membrane-bound EGFR is believed to be both clathrin-mediated and clathrin-independent.[27−29] The subsequent translocation of EGFR from endocytic vesicles to the nucleus has been proposed to proceed through several potential mechanisms, all of which involve an interaction between EGFR and the karyopherin family of nuclear transport proteins.[23,25,30−33]

In this study, photoactive NPs composed of a Fe_3O_4 core and a TiO_2 shell ($Fe_3O_4@TiO_2$) were surface conjugated with several different peptides to form peptide nanoconjugates (NCs) and tested for binding to EGFR and the ability of NC-EGFR complexes to interact with karyopherin-β. NCs performing most similarly to a native EGFR ligand (i.e., interacting most avidly with EGFR and karyopherin-β) were selected for cellular uptake experiments. After a 30 min interaction with cells, some of these EGFR-targeted NCs reached cell nuclei, although many remained in the cytosol. As a control, we used NCs that could enter cells but not cell nuclei. NC presence in the nucleus improved photo-activation-dependent nuclear DNA cleavage.

The localization of EGFR-targeted NCs was confirmed with X-ray fluorescence tomography. While X-ray fluorescence tomography has been done before with sub-micrometer resolution on dried samples at room temperature,[34] this study is the first example of cryogenic X-ray fluorescence tomography with an X-ray beam focused below 100 nm. This work was done at the Bionanoprobe, a unique instrument for X-ray fluorescence microscopy located at the Advanced Photon Source at Argonne National Laboratory (APS-ANL).

RESULTS

Synthesis of EGFR-Binding $Fe_3O_4@TiO_2$ Nanoconjugates. NPs used in this work were made of an Fe_3O_4 core and TiO_2 shell ($Fe_3O_4@TiO_2$ NPs), for a final NP size of 6.7 ± 2.9 nm (for details see Supplementary Methods, Supplementary Figure S1, and Supplementary Table S1).[35] The main advantage of this combination of materials over pure TiO_2 is that the presence of Fe_3O_4 core particles decreases the band gap of TiO_2, making NPs excitable with white light.[36]

Several peptides that purportedly bind with EGFR[37−39] as ligands and additional control peptides were conjugated to the surface of $Fe_3O_4@TiO_2$ NPs (for details see Methods, Supplementary Methods, Supplementary Figures S1, S2, and Supplementary Table S1) to form peptide nanoconjugates. We then tested interactions between these NCs and EGFR in a protein pulldown assay (Supplementary Figure S3). An 11 amino acid peptide fragment of epidermal growth factor[37] called B-loop peptide performed the best in binding of EGFR; this peptide was used for all subsequent work. A scrambled version of the B-loop peptide with a rearranged amino acid sequence called scrambled peptide was used to prepare a matching negative control. Both of these peptides were conjugated to the surface of $Fe_3O_4@TiO_2$ NPs using an N-terminal 3,4-diphenylacetic
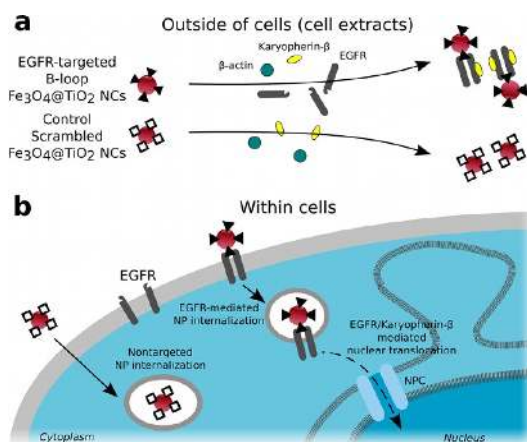

Figure 1. Schematic representation of findings presented in this work. Both EGFR-targeted B-loop and control scrambled NCs were tested for interactions with EGFR and other proteins from (a) cell extracts and (b) within HeLa cells. (a) NCs carrying B-loop peptides were shown to bind and pull down EGFR and the nuclear transport protein karyopherin-β (Figure 2a, Supplementary Figure 3). (b) Cellular uptake and distribution of nanoconjugates were shown by flow cytometry (Figure 2b and c, Supplementary Figures S4 and S5), confocal microscopy (Figure 3, Supplementary Table S2), X-ray fluorescence microscopy (Figure 4, Supplementary Table S3, Supplementary Figure S7), and cryo-X-ray fluorescence microscopy with the Bionanoprobe (Figures 5 and 6, Supplementary Video, and Supplementary Figures S8−S13). In the absence of EGFR nuclear transport inhibitors, and after a 30 min incubation at 37 °C to allow endocytosis, photoactivation of the EGFR-targeted B-loop NCs caused increased DNA degradation compared to control NCs and treatment conditions (Figure 7, Supplementary Figures S14 and S15). NPC: nuclear pore complex.

acid moiety (DOPAC) (for more details see Methods, Supplementary Methods, and Supplementary Figures S1, S2, and S3). The orthosubstituted enediol groups on DOPAC as well as other catechols can stably bind to surface TiO_2 molecules on NPs.[4,40−42] These B-loop and scrambled peptide nanoconjugates (B-loop NCs and scrambled NCs) were used side by side for all experiments described here (schematically presented in Figure 1).

Cellular Protein Pulldown with EGFR-Binding Nanoconjugates. The first step in deciding whether B-loop NCs would be able to reach the cell nucleus was to investigate the interaction between NCs, EGFR, and the nuclear translocation protein karyopherin-β. This was done by a pulldown assay we devised for this purpose (Figure 2; described in Methods, Supplementary Methods, and Supplementary Figure S3).

B-Loop NCs bind and pull down EGFR from the cell extracts of HeLa cells, while bare NPs and scrambled NCs did not (Figure 2a, Supplementary Figure S3). Complexes made of EGFR and B-loop NCs moreover bind the nuclear transport protein karyopherin-β (Figure 2a, Supplementary Figure S3). In general, NPs can accumulate a protein corona through polar and other nonspecific interactions;[43,44] however, in this case, none of the proteins tested by Western
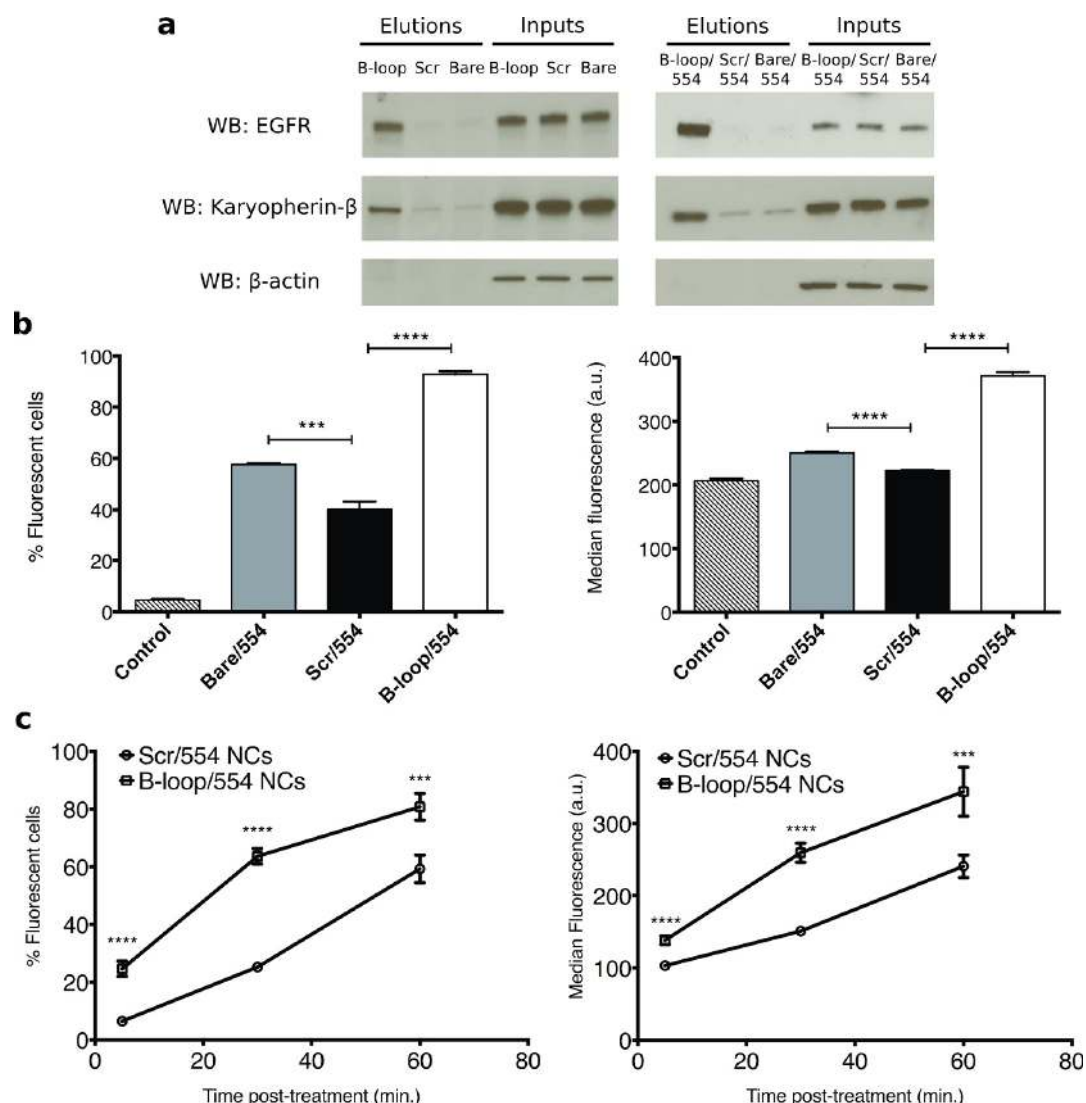
Figure 2. B-Loop NCs, but not control scrambled NCs, bind EGFR and karyopherin-β from cell protein extracts and show increased internalization within HeLa cells. (a) Western blots (WB) of proteins eluted from NCs used for protein pulldown from HeLa cell extracts (Elutions) show specificity of interaction between EGFR and B-loop modified NCs (B-loop). No such interaction occurs between scrambled NCs (Scr) or bare NPs (Bare). Loading of a portion of the whole cell protein extract used for pulldown reactions (Inputs) shows equal protein concentrations prior to pulldown interaction. The flow-through (FT) and wash fractions (W1, W2, W3) are shown in Supplementary Figure S3. Addition of the fluorescent dye DY554 (/554) to the particle surface (right-hand panels) did not change the behavior of NCs. Karyopherin-β coeluted with EGFR only when B-loop NCs were used. (b) Flow cytometry analysis of HeLa cells treated with the same NCs used (a) for 30 min at 37 °C. (c) Flow cytometry of HeLa cells treated with B-loop or scrambled NCs for different periods of time at 37 °C. While uptake of both NCs increased over time, EGFR-targeted B-loop NCs were always endocytosed more efficiently. Error bars represent standard error of the mean ($n = 3$), **$p < 0.01$, ***$p < 0.001$, ****$p < 0.0001$.

blot (EGFR, karyopherin-β, and β-actin) adsorbed non-specifically on bare NPs or scrambled NCs. The interaction between B-loop NCs and karyopherin-β should be mediated *via* EGFR and not by a direct interaction between B-loop peptides and karyopherin-β. This nuclear transport protein preferentially binds to nuclear localization signal (NLS) sequences composed of basic amino acids,[45] such as the tripartite NLS in the intracellular domain of EGFR.[31] Binding with karyopherins is necessary for the translocation of ligand-bound EGFR to the nucleus.[25,30,33,46,47] Moreover, this interaction depends on phosphorylation of a specific threonine residue: Thr654.[26]

For that reason, phosphorylated EGFR NLS peptides can be used to inhibit EGFR nuclear translocation;[22,26] we used the same strategy in subsequent NC comet assays (Figure 7b).

Cellular Uptake of EGFR-Binding Nanoconjugates. Ligand-bound EGFR is rapidly internalized and can be expected to migrate into the cell nucleus within 30 min after interaction with its ligand.[23,30,31] In order to follow the accumulation of B-loop NCs, scrambled NCs, or bare NPs in HeLa cells, we labeled these NCs with the fluorescent dye DY554. Addition of this dye did not alter NC interactions with EGFR and karyopherin-β

from cell extracts (Figure 2a). The internalization of DY554-labeled NCs by HeLa cells was evaluated by flow cytometry (Figure 2b and c). A low percentage of "fluorescence positive" cells was noted in untreated cells; cells treated with "bare" NPs modified only with DY554 demonstrated some nanoparticle uptake after a 30 min incubation at 37 °C, as shown by an increase in both the percent of fluorescent cells and an increase in the median fluorescence of gated cells (Figure 2b; dot plots and fluorescence histograms are shown in Supplementary Figure S4). A similar finding with fluorescently labeled TiO_2 NPs was previously reported by our group;[48] these nontargeted TiO_2 NPs formed numerous nonspecific interactions with cells, leading to their uptake by any endocytic mechanism ongoing in the cells. Internalization of scrambled NCs by HeLa cells shown here most likely proceeded by similar mechanisms. B-Loop NCs demonstrated the greatest uptake at the 30 min time point, showing a significant increase in both the percentage of fluorescent cells and the median fluorescence (Figure 2b); example dot plots and fluorescence histograms for these samples are given in Supplementary Figure S4.

The uptake of B-loop NCs *vs* scrambled NCs showed preferential uptake of B-loop NCs at time points between 5 min and 1 h (Figure 2c); example dot plots and fluorescence histograms for these samples are given in Supplementary Figure S5.

It is noteworthy that in flow cytometry experiments the presence of NPs anywhere in the cell was detected, regardless of whether they are in the cytoplasmic endosomes or the cell nucleus.

Tracking the Subcellular Distribution of Nanoconjugates by Confocal Microscopy. To investigate the subcellular distribution of internalized NCs, we used confocal microscopy experiments (Figure 3). The primary focus of these experiments was to establish whether B-loop NCs can be found in the cell nucleus within a similar time frame (30 min) as EGFR bound with its native ligands.

At the 0 min time point, HeLa cells were treated with scrambled or B-loop NCs at 4 °C to allow for receptor binding but not endocytosis (SNC 0 min and BNC 0 min). Cells were fixed and poststained for nuclear DNA (using Hoechst) and EGFR, while the NCs were poststained with alizarin red S (ARS), a dye that preferentially binds TiO_2 NPs.[48,49] EGFR was immunolabeled with a primary antibody that binds the carboxy terminus of the receptor, which was then fluorescently labeled with AlexaFluor488-conjugated secondary antibodies. Since ligand binding occurs at the extracellular amino terminus of the receptor, the presence of NCs should not interfere with antibody binding. B-loop NCs (arrowheads) and to a lesser degree scrambled NCs (dashed arrows) co-localize with EGFR at the cell membrane at 4 °C (Figure 3a).

For the 30 min time point, the cells were again pretreated with B-loop or scrambled NCs at 4 °C, but these cells were then incubated at 37 °C for 30 min to allow for endocytosis and intracellular trafficking (SNC 30 min or BNC 30 min). At this time point, ARS-stained B-loop NCs were found in both the cytoplasm and the cell nucleus (Figure 3a bottom panel and Figure 3b), while scrambled NCs remained solely in the cytoplasm (Figure 3c). Both the nuclear and the cytoplasmic ARS-labeled B-loop NCs still appear to co-localize with AlexaFluor488-labeled EGFR. The presence of EGFR-associated B-loop NCs in the cytoplasm as well as in the nucleus after 30 min is expected because in all cell systems studied so far only a fraction of activated EGFR translocates into the nucleus.[18,21,23,26,30−33,46,50] In addition to the fact that different ligands or cell stresses have different effects on EGFR nuclear trafficking, nuclear accumulation of EGFR in different cell types is variable as well.[9,13,14,20,24,51−53] In one specific example nuclear accumulation of EGFR was found to be around 2% of total cellular EGFR.[54]

Direct Determination of Nanoconjugate Subcellular Distribution by XFM. As a complementary technique to confocal microscopy, we used X-ray fluorescence microscopy (XFM) to confirm the subcellular distribution of $Fe_3O_4@TiO_2$ NPs and NCs. While NPs must be fluorescently labeled to be detected by confocal microscopy, XFM can detect NPs *via* the X-ray-induced X-ray fluorescence of the Fe and Ti atoms within NPs.[4,35,48,55]

XFM (also called Synchrotron radiation induced X-ray emission, or SRIXE) can also be used to map the distribution of naturally occurring cellular elements such as phosphorus (P) and sulfur (S) or trace metals such as copper (Cu) and zinc (Zn) and has been used with a variety of biological and biomedical samples.[4,56−58] Elemental content of cells can be used not only to establish physiological processes ongoing in cells but also to delineate different subcellular compartments such as mitochondria (rich in manganese) or cell nuclei (presenting the highest concentration of P and Zn).[4,55,58,59] Sulfur, on the other hand, is present in the amino acids methionine and cysteine and is therefore distributed throughout the cell in all cellular proteins.[55,56,59] While some native cellular elements are occasionally present in cells in extremely small quantities, metallic nanomaterials in treated cells are often relatively abundant and can be detected with high sensitivity and without staining by XFM. In addition, immunocytochemisty with gold (Au)-conjugated antibodies can easily be paired with XFM to detect a particular protein of interest.[60] In recent years, attempts were made to use elemental X-ray imaging to obtain not only a 2D map but a 3D tomographic reconstruction of elemental distribution in biological samples. An early example of such effort was the work by de Jonge and others, who manually rotated an air-dried diatom to record a tilt series of 2D elemental maps with
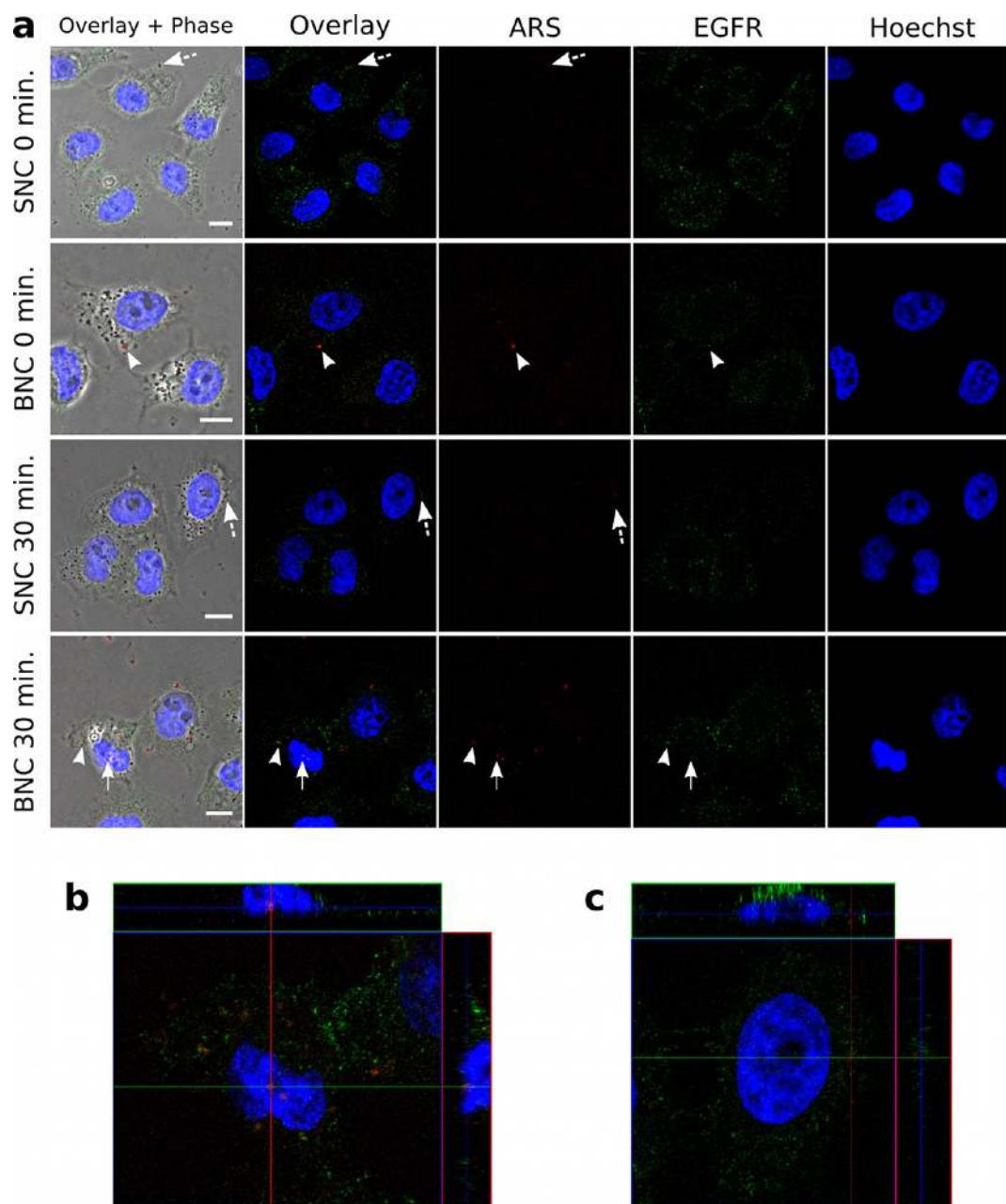
Figure 3. B-Loop NCs co-localize with EGFR at the cell membrane and within the cell nucleus at different time points. (a) HeLa cells were treated with 10 nM B-loop NCs (BNC) or scrambled NCs (SNC) at 4 °C for 1 h to allow for receptor binding. Cells were then left at 4 °C (BNC 0 min or SNC 0 min) or shifted to 37 °C (BNC 30 min or SNC 30 min) for 30 min to allow for endocytosis. EGFR was labeled with AlexaFluor-488 conjugated antibodies (green), nuclear DNA was stained with Hoechst (blue), and NCs were stained with alizarin red S (ARS) (red). Most pronounced NC staining and co-localization with EGFR were at the cell periphery (arrowhead) in cells treated at 4 °C, while in cells allowed to endocytose NCs at 37 °C the staining for B-loop NCs overlaps with EGFR in both the cytoplasm (arrowhead) and the cell nucleus (arrow). Images show single focal planes from representative Z-stacks. (b) Orthogonal projections of the BNC 30 min cell, confirming the location of ARS-stained NCs within the Hoechst-labeled nucleus in the XY (middle), YZ (top), and XZ (right) planes. In contrast, scrambled NCs remained predominantly at the cell periphery (a, dotted arrow) after 30 min (c, orthogonal projections), although there is random co-localization with EGFR. The X, Y, and Z resolutions of the images are 0.082 μm × 0.082 μm × 0.38 μm (SNC 0 min); 0.057 μm × 0.057 μm × 0.38 μm (BNC 0 min); 0.071 μm × 0.071 μm × 0.38 μm (SNC 30 min); and 0.070 μm × 0.070 μm × 0.38 μm (BNC 30 min). Manders' correlation coefficients for co-localization between ARS-labeled NCs to AlexaFluor488-labeled EGFR are given in Supplementary Table S2. Scale bars: 10 μm.

an X-ray beam of a few hundred nanometers.[34] This data set was then reconstructed into a 3D tomogram of elemental distribution in the diatom shell and its dried internal content.

Because of our focus on the spatial relationship between B-loop NCs and EGFR within cancer cells, we labeled EGFR with 1.5 nm Au conjugated antibodies to map the distribution of EGFR. In HeLa cells
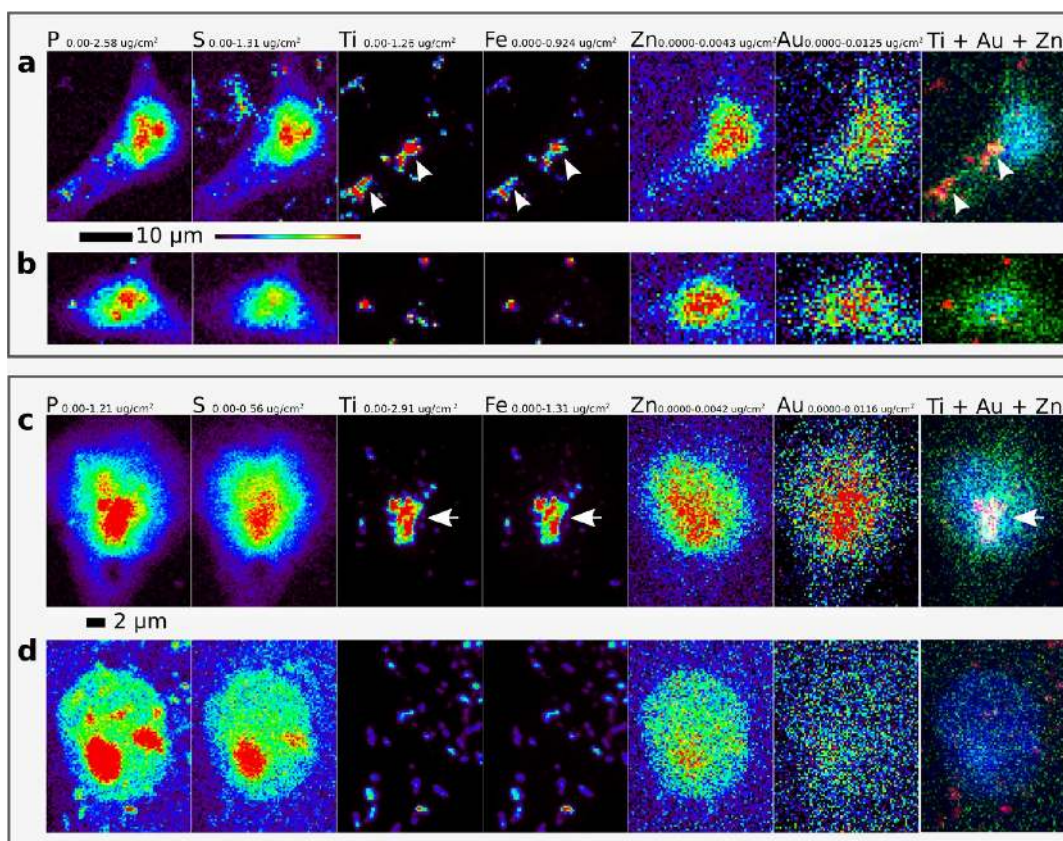
Figure 4. XFM reveals the distribution of NCs in HeLa cells after 0 or 30 min incubation at 37 °C. (a) In HeLa cells treated with B-loop NCs at 4 °C the NCs (Ti and Fe elemental maps) are distributed at the cell periphery and overlap with strong signals in the elemental map for Au, which indicates distribution of Au-labeled anti-EGFR antibodies (arrowheads). (b) Ti and Fe from scrambled NCs are also distributed at the cell periphery but overlap less with Au. Scale bar: 10 μm. (c) Ti and Fe signals from B-loop NCs overlap both with Zn, which is enriched in the cell nucleus, and with EGFR-specific Au in a cell treated with B-loop NCs at 37 °C for 30 min (arrows). (d) Conversely, in a cell treated with scrambled NCs for 30 min at 37 °C, the Ti and Fe distributions remain separate from the Zn and Au signals. Three cells were scanned per treatment group with images of representative cells shown. Scale bar: 2 μm. Panels represent 2D maps of the distributions of phosphorus (P), sulfur (S), titanium (Ti), iron (Fe), zinc (Zn), gold (Au), and the three-element co-localization of Ti (red), Au (green), and Zn (blue). Manders' coefficients for the correlation between Ti and Fe, Au, or Zn as well as scatter plots of the distributions of these elements are given in Supplementary Table S3 and Figure S7.

treated at 4 °C with B-loop NCs (Figure 4a) or scrambled NCs (Figure 4b), the distribution of Ti and Fe elements, indicating distribution of NCs, favors the periphery of the cells, similar to the situation noted in Figure 3a. It should be noted that, while the native cellular iron content is above background level (Supplementary Figure S6), the distribution pattern of pixels with the highest iron content in NC-treated cells always replicated distribution of titanium because of the core—shell formulation of NPs. This is also apparent from "control" Manders' coefficients for co-localization of Ti and Fe in NC-treated cells (Supplementary Table S3).

In the cytoplasmic region of the 0 min B-loop NC treated cells there are regions where the EGFR-specific Au signal and the Ti and Fe signals overlapped, indicating that these NCs co-localized with EGFR (Figure 4a, arrowheads). Similar to the confocal microscopy images, after 30 min of incubation at 37 °C (30 min), XFM images also indicated the presence of B-loop NCs in the cytoplasm and nucleus of

HeLa cells, co-localized with EGFR in both locations (Figure 4c). In 30 min scrambled NC treated cells Au-labeled EGFR demonstrated little overlap with NCs (Figure 4d). Scatter plots indicating co-localization of Ti from NCs and nuclear Zn as well as co-localization of Ti and EGFR-specific Au are given in Supplementary Figure S7 and the Manders' coefficients in Supplementary Table S3.

High-Resolution, Cryogenic, and Tomographic XFM Imaging of NC-Treated Cells at the Bionanoprobe. To determine the location of NCs within cells with greater accuracy, we used the recently installed Bionanoprobe instrument, located at APS-ANL at the Life Sciences-Collaborative Access Team sector 21-ID-D. The Bionanoprobe is the first and only XFM instrument that allows imaging of frozen-hydrated biological samples up to 10−20 μm thick, with an X-ray beam that can be focused to 30 nm. Imaging of frozen-hydrated cells under cryogenic conditions is a reliable way to preserve the architecture of the cell and minimize rearrangement or loss of
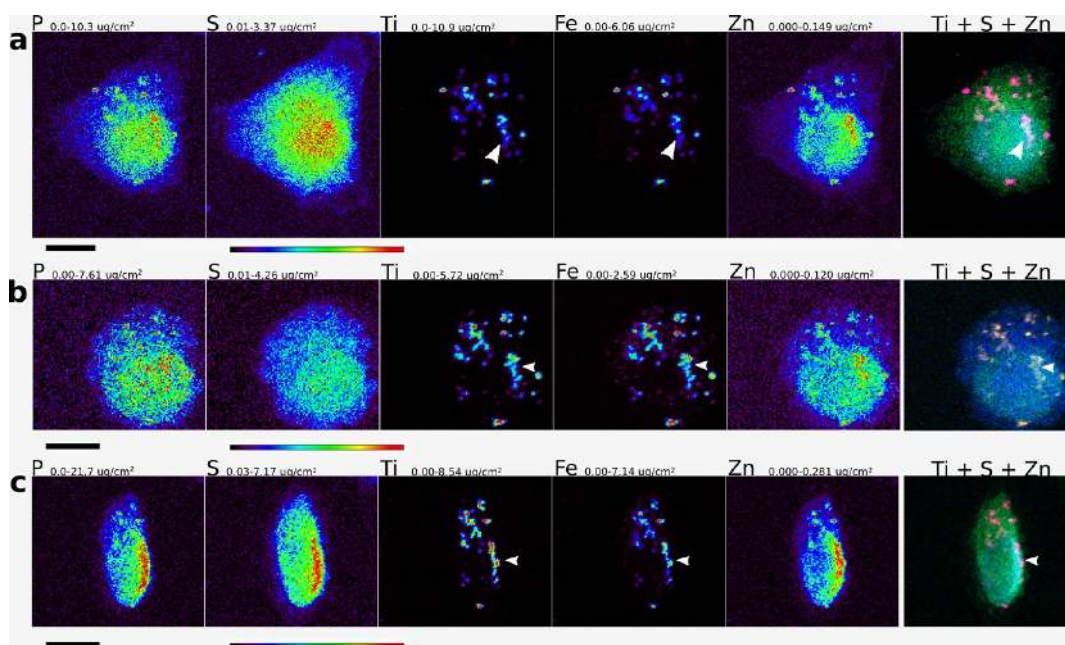
Figure 5. High-resolution Bionanoprobe images of frozen-hydrated HeLa cell treated with B-loop NCs at 4 °C at multiple angles. An X-ray beam spot size of 50 nm allowed acquisition of a detailed image of a HeLa cell treated with B-loop NC at 4 °C. The majority of NC hot spots were distributed at the cell periphery. (a) In some cases, the apparent distribution of Ti and Fe overlapped with nuclear-specific P and Zn signals. After rotating the cell over a range of 144 degrees (in 6-degree increments) it was possible to determine that NC hot spots that appeared nuclear in some projections (a and b) are in fact extranuclear when the cell is scanned at an angle of 60 degrees (c, arrowheads). Each panel represents a different elemental map; from left to right: phosphorus (P), sulfur (S), titanium (Ti), iron (Fe), zinc (Zn), and a three-element co-localization of Ti (red), S (green), and Zn (blue). Images obtained at all other angles are provided in Supplementary Figure S8. Scale bars: 10 μm.

diffusible ions.[61] While cryo TEM shares these benefits, it requires sectioning of cells, whereas cryo XFM allows tomographic imaging of intact, whole cells. Three-dimensional imaging of elemental content in frozen-hydrated cells at the Bionanoprobe is supported *via* a specimen stage that can be rotated by $\pm 80°$. This custom-made instrument was designed and manufactured by Xradia (now Carl Zeiss X-ray Microscopy), installed and commissioned at the APS over the past 20 months. During this period of instrument development we were able to use it to image some of the HeLa cells treated with B-loop or scrambled NCs. These specimens were plunge-frozen and scanned in a frozen-hydrated state with a beam spot size of 70 nm.

Cells treated with B-loop NCs at 4 °C were imaged at scan angles between −66 and 78 degrees in six-degree increments. Several key angular projections are shown in Figure 5, with the remaining projections shown in Supplementary Figure S8. The high sensitivity and high detail visible with the Bionanoprobe allow one to see accumulations of NPs that would be difficult to resolve with a wider beam spot. In addition, scanning the same cells at different angles allowed us to discern that some of the NC aggregates seemingly inside the cell (arrowheads) were only attached to the cell surface (Figure 5).

We also scanned frozen-hydrated HeLa cells treated with B-loop or scrambled NCs for 30 min at 37 °C at the Bionanoprobe (Figure 6). Again, the rotation of the sample and acquisition of elemental projection images at multiple angles allowed us to confirm that in B-loop NC treated cells the Ti and Fe hot spots that appear to be in the nucleus appear so at every scan angle (Figure 6a−c, Supplementary Figure S9, and Supplementary Video). Three-dimensional tomographic reconstructions of this cell show that the NC aggregates labeled NC 4 and NC 5 localize to the Zn-rich nucleus region (Figure 6d, Supplementary Figure S10, and Supplementary Video). In the tomographic reconstruction the Zn signal can be used as a proxy for the general size of the nucleus, as Zn content has been shown to be elevated in the nucleus.[58,59] In contrast, NC aggregates NC 2 and NC 3 are distributed in the perinuclear compartment, while NC 1 is associated with extranuclear Zn within the cytoplasm (Supplementary Figures S9 and S10 and Supplementary Video). One of the images from the tilt series (Supplementary Figure S11) was used to quantify the Ti content of different aggregates (NC 1−5). On the basis of this quantification, the two nuclear NC aggregates NC 4 and NC 5 account for 21.1% of the Ti content of this cell.

In contrast, scrambled NC treated cells showed no nuclear NC presence. Whenever it appeared that these NCs were in the nucleus when the cell was observed at one rotation angle, it was later found under additional angles that the location of scrambled NCs was extranuclear (Figure 6e,f, Supplementary Figure S12).

Finally, scanning of several cells at the same angle before and after sample rotation and extended
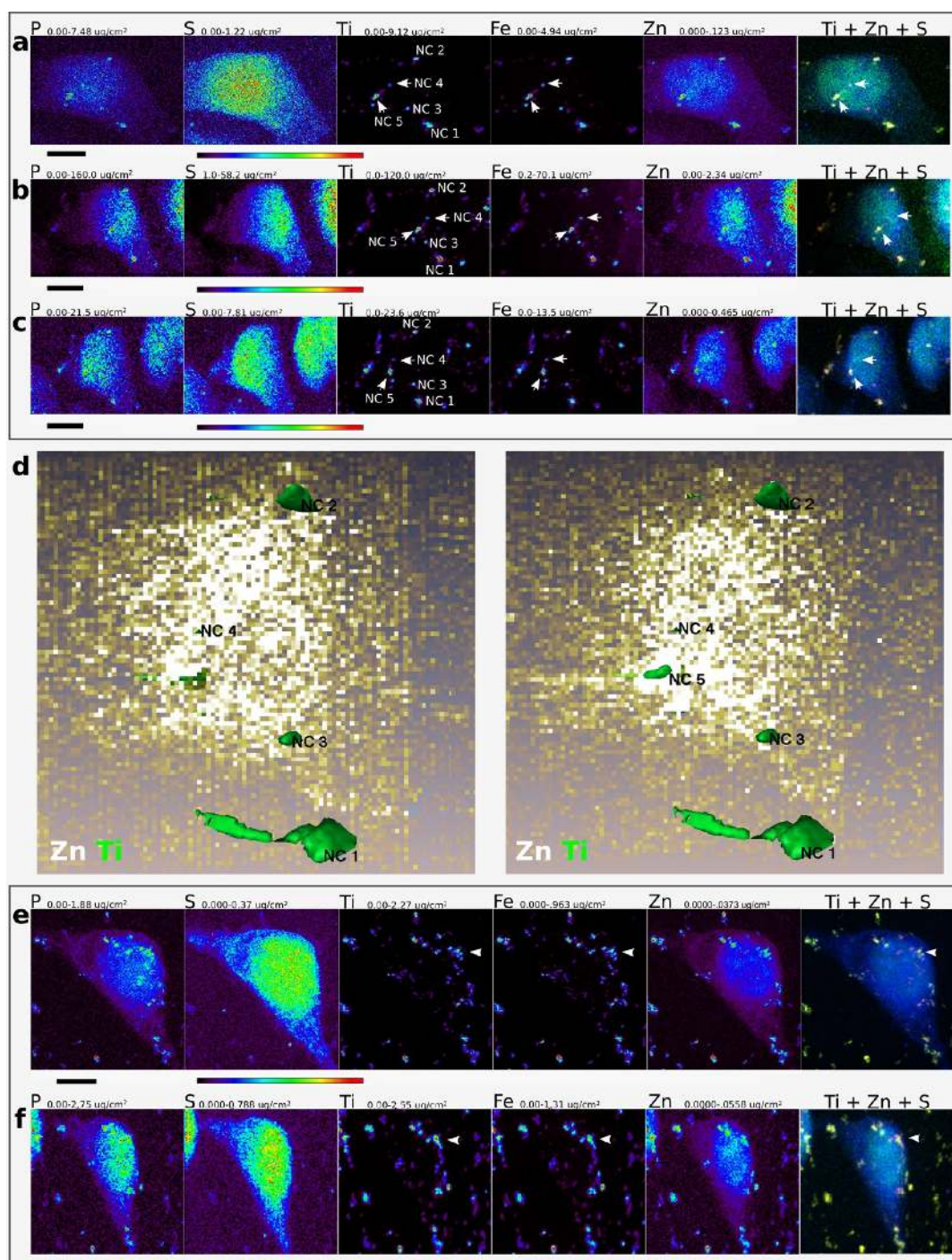
Figure 6. Bionanoprobe images and tomographic reconstructions of frozen-hydrated HeLa cells treated with NCs for 30 min at 37 °C. (a) In a cell treated with B-loop NCs at 37 °C for 30 min the presence of NCs (represented by Ti and Fe signals) can be seen both in the cytoplasm (NC 1, NC 2, and NC 3 localize to regions with distinct S signal and weak P and Zn signals) and in the nucleus (NC 4 and NC 5 localize to areas with strongest Zn and P signals) at a scan angle of 0 degrees. The same cell was rotated, and the two NC hotspots (NC 4 and NC 5) overlapping with nuclear Zn remain overlapped with Zn at (b) 54 degrees and (c) −60 degrees. All angular projections of this cell are shown in Supplementary Figure S9. (d) Tomographic reconstructions of the cell in (a)−(c) showing the XY orthoslice of the Zn distribution (white) and an isosurface representation of the Ti distribution (green). The two NC hot spots labeled NC 4 (left panel) and NC 5 (right panel) clearly co-localize with the nuclear Zn signal. Additional tomographic reconstructions are shown in Supplementary Figure S10 and the Supplementary Video. (e, f) Under the same treatment conditions, scrambled NCs do not localize to the nucleus. While at a scan angle of 6 degrees the Ti and Fe signals appear to co-localize with nuclear Zn (arrowhead), a scan of the same cell at 54 degrees (f) shows the Ti and Fe signals to be in an area directly above the nucleus within the cytoplasm. All angular projections of the cell in e are shown in Supplementary Figure S12. At the end of the tilt series, cells in (a) and (e) were scanned again at 0 and 6 degrees, respectively, to show that there were no morphological changes due to data collection (Supplementary Figure S13). Scale bars: 10 μm.

X-ray beam exposure was done in order to evaluate if X-ray beam exposure led to sample degradation (Supplementary Figure S13). The morphology of the nucleus and cytoplasm (indicated by elemental distribution of Zn, S, *etc.*) as well as nanomaterial distribution was not changed between scans.

DNA Degradation Evaluation by Comet Assay. Activation of TiO_2 with photons of wavelengths smaller than 388 nm leads to the formation of free electrons and electropositive holes that can then generate reactive oxygen species (ROS) within the local environment of the NP.[3,62] TiO_2 NPs doped with iron have an even more narrow band gap and can be photoactivated with light wavelengths of 350−450 nm depending on the ratio between Fe and Ti.[63,64] $Fe_3O_4@TiO_2$ NPs such as the ones used in the current work can also be activated with white light.[36] Within cells, ROS can lead to lipid peroxidation, protein denaturation, and DNA damage, any of which can have cytotoxic effects.[65] However, it has also been shown that ROS cannot travel farther than 1.1 μm away from the NP itself in an aqueous environment[5] and that within cells hydroxyl radicals have a diffusion distance of only 60 Å.[66] Therefore, successful delivery of NCs to cell nuclei followed by light activation can be expected to cause more DNA damage than the delivery of NCs to the cytoplasm or perinuclear region. As a corollary, NP activation after a completed nuclear delivery of B-loop NCs (incubation at 37 °C in the absence of inhibitors of EGFR nuclear translocation) should cause more DNA cleavage than photoactivation of any of the following: scrambled NCs or B-loop NCs incubated with cells at 4 °C or in the presence of EGFR nuclear translocation inhibitors.

We evaluated DNA damage induced by photoactivation of NCs using a neutral comet assay protocol developed by Olive and others,[67,68] also known as single-cell gel electrophoresis assay (Figure 7). The neutral comet assay can be used to measure double-strand DNA breaks over a range of 50 to 10 000 breaks per cell.[67] In addition, heterogeneity in comet appearance is associated with DNA cluster damage, which is often seen after irradiation with heavy ions that can cause multiple double-strand DNA breaks in close proximity.[69] Several approaches for graphic representation of comet assay data are in use;[67,68,70,71] we present our data using all of these approaches. In Figure 7 we present the data in its simplest form: as percent of total DNA in the comet tail, averaged for all the cells exposed to the same treatment. Olive tail moments (Supplementary Figure 14) provide a measure of both % DNA in the comet tail and the tail length.[67,68] While this representation of the data is more informative, it does not allow a direct comparison between treatments with different types of DNA-damaging agents, and thus, positive controls used in this work could not be directly compared with the NC

treatments. Finally, Supplementary Figure S15 gives each individual cell's percent tail DNA plotted against total cell fluorescence. This representation of the data demonstrates variability of accumulated DNA damage, particularly in cells with NCs inside nuclei. On one hand, NCs inside nuclei are more likely to cause clustered DNA damage than more distant NCs in the cytoplasm (considering an average travel distance of 60 Å for ROS inside cells, we can assume that only a fraction of the ROS produced by cytoplasmic NCs reaches the nucleus). On the other hand, variability in DNA damage may also be a reflection of cell-to-cell variability in the quantity of NCs inside nuclei.

Figure 7a (and Supplementary Figures S14 and S15) shows results of NP activation in cells illuminated with white light for 10 min after they were treated with no NPs, 10 nM B-loop NCs, or 10 nM scrambled NCs. At the outset of this experiment, all cells were treated at 4 °C for 30 min to allow for NC-EGFR binding, but not endocytosis. Samples were then separated and some remained at 4 °C, while others were incubated at 37 °C for 1 h to allow for nuclear translocation. After incubation, cells at both incubation time point were either illuminated with a 150 W halogen lamp under a thin layer of PBS for 10 min to photoactivate NCs or kept in the dark. Cells were immediately embedded in agarose and processed according to the neutral comet assay procedure.[67]

Figure 7b (and Supplementary Figures S14 and S15) shows comet assay results of scrambled NCs and B-loop NCs cell treatments in the presence or absence of 10 μM dasatinib or 5 μM competitor EGFR-NLS-phosphopeptide. Both of these treatments have been used to prevent translocation of EGFR into the cell nucleus.[22,24,26,52,72] While dasatinib acts as an inhibitor of c-Src kinases and prevents EGFR nuclear translocation through this mechanism, EGFR-NLS-phosphopeptide binds to and overwhelms the nuclear import machinery responsible for nuclear accumulation of EGFR. In this set of experiments illumination was done with UV light over a period of 8 min (0.8 J/cm²). Even under this relatively extensive illumination (sufficient to lead to DNA unwinding in cells that were illuminated in the absence of NCs) B-loop NC treated cells in the absence of inhibitors developed comets with a significantly higher percent DNA tail than any of the other samples. A similar experiment done with a shorter UV illumination (3 min, corresponding to 0.3 J/cm²), shown in Supplementary Figures S14 and S15, shows no difference between nontreated nonilluminated cells and control-treated samples; however, following this treatment a significant increase in DNA damage occurred in B-loop NC treated and illuminated cells.
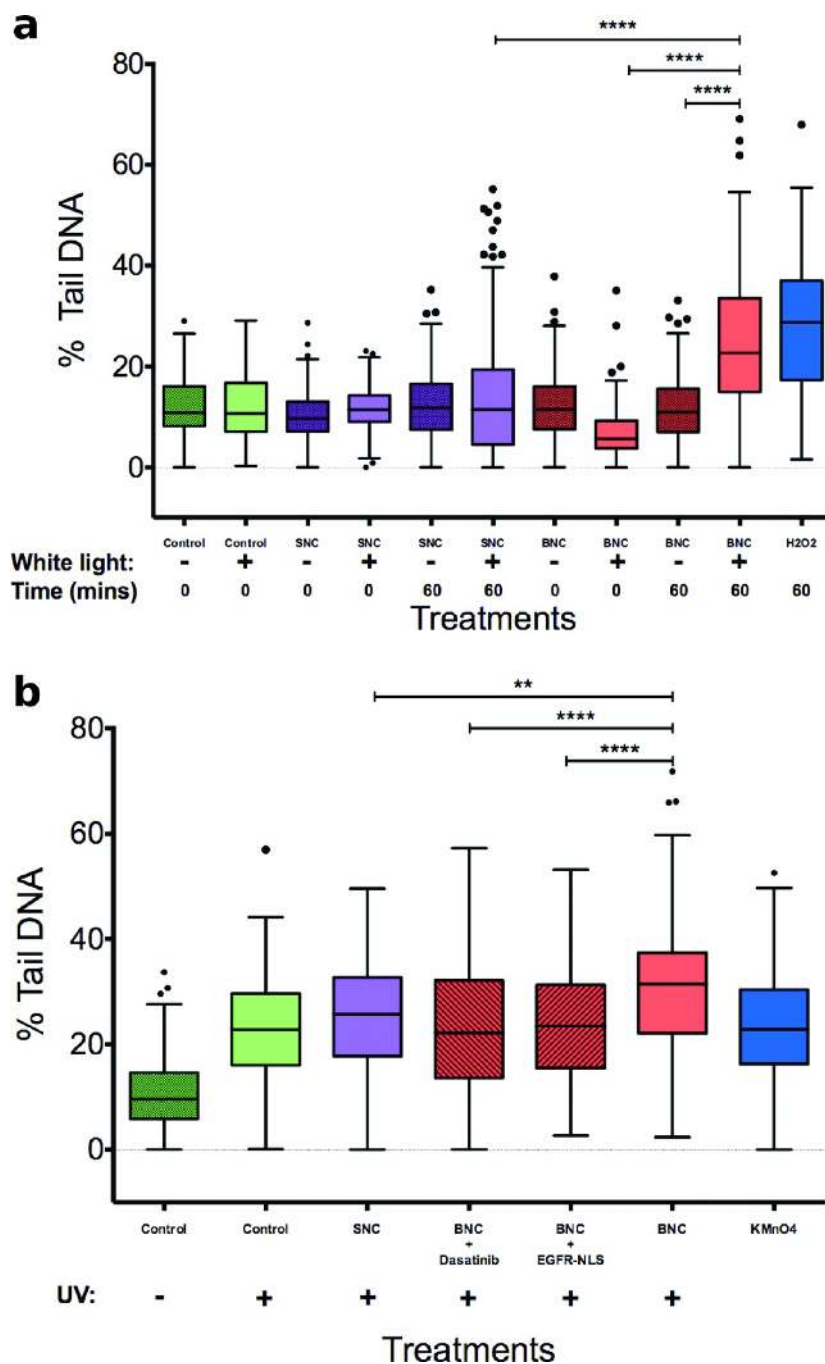
Figure 7. Light activation of NCs inside cells leads to DNA degradation, most pronounced in cells treated with B-loop NCs in the absence of inhibitors of EGFR nuclear transport. NC-treated cells were either (a) exposed to white light or (b) UV illuminated. Immediately after illumination cells were embedded in low melting point agarose and subjected to neutral lysis. Following electrophoresis, cellular DNA was stained and imaged and comet tails were evaluated using CASP software.[73] The data are displayed as percent DNA in the tail. Box height represents the interquartile range (IQR); the centerline, the median; the whiskers, 1.5 times the IQR; and dots represent values greater than the IQR. **** = $p < 0.0001$, ** = $p < 0.01$. (a) Cells treated with B-loop NCs, scrambled NCs, or no NPs for 60 min at 37 °C (60) or only at 4 °C (0) were either illuminated with white light (+) for 10 min or kept in the dark (−). Cells treated with 880 μM H_2O_2 were included as a positive control. (b) HeLa cells untreated or pretreated with inhibitors of EGFR nuclear transport (10 μM dasatinib and 5 μM EGFR-NLS phosphopeptide) were treated with B-loop NCs, scrambled NCs, or no NPs for 30 min at 37 °C. Illumination with UV light over a period of 8 min (0.8 J/cm²) was done, and the cells were immediately embedded and processed. Cells treated with 25 μM $KMnO_4$ were included as a control.

DISCUSSION

Many strategies for cellular targeting have employed different EGFR-targeting ligands and moieties such as whole EGF,[74,75] EGF fragments,[37,38] EGFR-binding peptides,[76] or anti-EGFR antibodies.[77] However, the specificity of EGFR-targeted delivery remains controversial because of the ubiquitous presence of this receptor and its important role in maintaining the

health of normal tissue. The NCs shown here utilized interactions with EGFR to not only enter cells but also translocate to the cell nucleus. Other peptides (and peptide-conjugated nanoconstructs) known to enter cells and translocate to the cell nucleus are most often constructed to carry the NLS sequence on their own.[78] Such peptides bind directly to the karyopherins, and some have been shown to allow NPs of up to 234 nm to translocate to the nucleus.[79] However, NLS carrying peptides cannot differentiate between cells of different nuclear EGFR status, while B-loop NCs from our current work utilize the native interaction between ligand-bound EGFR and karyopherin-β to enter the nucleus. Since the nuclear import of EGFR is associated with more aggressive cancers,[9,14,20,22,24,51−53,80] limiting NC delivery to the nuclei of such cells may be a more nuanced approach for NC delivery.

To demonstrate the translocation of B-loop NCs to cell nuclei, we used several complementary techniques, including cryogenic, tomographic high-resolution X-ray fluorescence microscopy at the Bionanoprobe. This instrument can scan frozen whole cells under cryogenic conditions, thus allowing for the study of native, hydrated architecture and elemental distribution. These frozen-hydrated samples can be imaged at the Bionanoprobe at multiple rotation angles to generate three-dimensional tomograms that will greatly improve our ability to pinpoint the location of NPs within cells. While XFM tomography has been achieved before with dry rigid samples at room temperature,[34] accurate hard X-ray 3D mapping of hydrated biological samples such as mammalian cells requires cryopreservation. Cryogenic handling of cell samples not only preserves intact cellular structures and elemental distribution but also protects the samples from radiation damage during data collection.[81] The Bionanoprobe can be used for imaging of frozen-hydrated samples at cryogenic temperatures; moreover, these samples are scanned with step sizes smaller by at least 1 order of magnitude compared to other XFM instruments. These capabilities complement analytical electron microscopy (EM), in that the Bionanoprobe can carry out elemental mapping at high resolution and high sensitivity in "thick" specimens, without degradation of spatial resolution through increased specimen thickness. Although analytical EM allows still higher spatial resolution and excellent visualization of specimen ultrastructure, it is effectively limited to thin sections on the order of about 100 nm (thus limiting quantitative studies).

Another indication of nuclear accumulation of B-loop NCs was the more extensive nuclear DNA cleavage in cells treated with NCs in the absence (but not presence) of EGFR nuclear transport inhibitors. In our previous work, we demonstrated that TiO$_2$ NPs can be photoactivated to cleave DNA in a cell-free environment.[4] In this study, we show that the Fe$_3$O$_4$@TiO$_2$ NPs functionalized by a B-loop peptide behaved as EGFR ligands and a fraction of the NCs could reach the cell nucleus. Activation of nuclear NCs by UV or white light led to significant localized DNA damage, resulting in double-strand DNA breaks. Therefore, one potential application of these nucleus-localizing NCs is photodynamic therapy given either intraoperatively or topically.

In addition, this targeting strategy could also be used to improve the delivery and therapeutic index of DNA-binding agents or topoisomerase inhibitors.[82,83] For example the DNA intercalating anthracycline doxorubicin could be more specifically delivered to the nucleus once attached to B-loop NCs. While we have shown previously that doxorubicin can bind directly to bare Fe$_3$O$_4$@TiO$_2$ NPs,[35] other chemotherapeutic agents that cannot bind directly to the NP surface can be attached via catecholamine linkers.

It should be noted that the TiO$_2$ nanoparticle surface is reactive and can be expected to engage in nonspecific protein binding,[43,44,84] even though the B-loop peptide coating governs specific interaction with the extracellular surface of EGFR. Others have found that in some cases accumulation of a protein corona on engineered NPs modulates their behavior.[85,86] Plasma protein accumulation on TiO$_2$ NPs of different shapes and sizes has been a major focus of many studies.[44,87,88] Therefore, before we can expect to replicate the findings shown here *in vivo* we will need to adapt the B-loop NCs for such use. One potential improvement is to decrease the aggregation of these NCs in solution, as this can lead to significant NC size polydispersity. In particular, larger NCs have been shown to interact with cells more via sedimentation,[89] which could alter the dosing characteristics both *in vitro* and *in vivo*.[90,91] The addition of surface moieties such as amphiphilic or hydrophilic polymers, known to improve NP stability and biocompatibility *in vivo*,[92] will be tested. These and other modifications should prevent or reduce nonspecific interactions of NCs, improve NC stability by decreasing aggregation, and provide that the B-loop peptides are exposed enough to secure the ligand-mimicking function of NCs.

CONCLUSIONS

We have shown that mimicking EGFR's native ligand can improve the cellular uptake and nuclear translocation of photoactivatable Fe$_3$O$_4$@TiO$_2$ NPs. Significantly, the nuclear accumulation of EGFR is especially prominent in cancer cells, where the activity of DNA-cleaving NCs would be most desirable. For example, nuclear EGFR is associated with increased resistance

to chemotherapy,[52] and nuclear EGFR levels are inversely correlated with survival in several types of cancer.[12,51,53] Therefore, co-opting EGFR's nuclear trafficking to deliver genotoxic NPs may be one strategy that can be used to treat more aggressive cancer cells.

METHODS

NP Synthesis and Characterization. Fe_3O_4@TiO_2 NPs were synthesized by a modified sol–gel method.[35] In brief, Fe_3O_4 cores were synthesized by stirring a mixture of $FeCl_2$ and $FeCl_3$ in 24 mmol of citric acid for 3 h at room temperature. The resulting solution was allowed to gel in static air at 50–70 °C for 12 h. Subsequently, the TiO_2 shell was added when iron oxide core particles were stirred at 4 °C with gradual addition of $TiCl_4$. Cores and core–shell NPs were sized by atomic force microscopy (AFM) on a Veeco Multimode V AFM operated in tapping mode (Supplementary Figure S1a,b). The concentrations of Ti and Fe were determined on an X Series II inductively coupled plasma-mass spectrometer (Thermo Scientific). NPs dialyzed in 10 mM sodium phosphate buffer pH 6 were used as "bare NPs" (for zeta potentials and more details see Supplementary Table S1).

NP Surface Functionalization. N-Terminal 3,4-diphenylacetic acid conjugated B-loop (DOPAC-MYIEALDKYAC-COOH) and scrambled (DOPAC-EAKLDYMCIYA-COOH) peptides were synthesized by the IBNAM Peptide Chemistry Core of Northwestern University. A schematic representation of conjugation is provided in Supplementary Figure S2; additional details about the peptide conjugation process are provided in the Supplementary Methods.

NCs used for experiments were synthesized as follows. The peptides were diluted to a concentration of 324 μM in 160 μL of dH_2O and then mixed vol:vol with 880 nM NPs in an oxygen-free atmosphere to yield a 30% NP surface coverage (more details are given in the Supplementary Methods subsection "Peptide and dye conjugation to NPs"). Conjugation was performed at 4 °C for 16 h, and free, unconjugated peptides were separated from functionalized nanoconjugates by centrifugation at 9000g for 10 min. NC pellets were resuspended in dH_2O or serum-free EMEM. NCs prepared in this manner were used to measure NCs' zeta potentials (Supplementary Table S1) and imaged by cryo transmission electron microscopy (Supplementary Figure S1c,d). Quantification of NP surface conjugated peptides was done by measuring the amount of unbound peptide in the supernatant (Supplementary Figure S3b). Peptide-carrying NCs in this work were used within 72 h after the beginning of the conjugation of peptides to NPs.

Cell Culture. HeLa cervical cancer cells were grown in EMEM supplemented with 10% fetal bovine serum and 1% penicillin/streptomycin at 37 °C and 5% CO_2. For immunofluorescence, cells were grown on LabTek II microscope slides (LabTek) at a density of 5 × 10^4 cells per slide; for X-ray fluorescence microscopy, HeLa cells were grown on 1.5 mm × 1.5 mm Si_3N_4 windows (Silson) at a density of 4000 cells per window.

For evaluation of NC uptake by flow cytometry and preparation of samples for comet assay, cells were treated with NPs after they reached 60% confluency one day after seeding.

In all cases cells were treated in serum-free EMEM with NCs at 10 nM final concentration.

Pulldown Assay and Western Blotting. HeLa cell protein extracts (for more details see Supplementary Methods, "Protein isolation and NC-protein pulldown experiments" subsection) were diluted to 2 mg/mL and either loaded on Western blots as the "Inputs" (Figure 1; Supplementary Figure S3a) or incubated, with mild agitation, with 352 nM B-loop NCs, scrambled NCs, or bare NPs for 2 h at 4 °C. Subsequently, the mixtures were centrifuged at 9000g for 10 min at 4 °C to pellet NPs with bound proteins; the supernatants were labeled "FT" (for flow through) (Supplementary Figure S3c). The pellets were then washed by resuspending in lysis buffer followed by centrifugation; this step was repeated two more times, yielding a total of three wash fractions (W1, W2, W3) (Supplementary Figure S3c). Following the last wash step, the pellets were resuspended in Laemmli buffer containing 2-mercaptoethanol and incubated at 95 °C for

10 min to elute proteins. The samples were centrifuged one final time, and the supernatants were collected and size separated by SDS-PAGE. EGFR was detected by a rabbit monoclonal antibody (Epitomics) diluted 1:5000 in TBST/5% nonfat dry milk. Karyopherin-β and β-actin were labeled by mouse monoclonal antibodies (Abcam and Cell Signaling, respectively) diluted 1:5000 in TBST/5% nonfat dry milk.

Flow Cytometry. Fluorescent DY554-DOPA (56 μM) was mixed 1:1 vol:vol with 0.51 μM NPs in dH_2O to yield an estimated NP surface dye coverage of 5% (for additional details see Supplementary Methods subsection "Peptide and dye conjugation to NPs"). B-Loop and scrambled peptides were conjugated to DY554 NPs as described above and in the Supplementary Methods.

HeLa cells were treated with 10 nM B-loop/DY554 NCs, scrambled/DY554 NCs, or DY554 NPs for 30 min at 4 °C to allow for receptor binding, but not endocytosis. Subsequently, treated cells were washed with acidic glycine (0.2 M glycine, 0.15 M NaCl, pH = 3.0) to remove NCs or NPs randomly adhering to the cell membrane. It has been our experience that nontargeted interactions between NPs and proteins persist after such a wash.[48] To allow for endocytosis and intracellular trafficking, treated and washed cells were then moved to 37 °C for 5, 30, or 60 min. After a final wash in acidic glycine buffer and then PBS, cells were harvested by trypsinization and fixed in a 4 wt % solution of formaldehyde in PBS for 10 min at 25 °C. Flow cytometry was carried out in PBS on a LSR Fortessa Analyzer (Becton-Dickinson) with an excitation wavelength of 552 nm and bandpass filter 585/615 nm for DY554-conjugated NPs/NCs. Gating and data analyses were done with FCS Express V3 software (De Novo Software).

Immunofluorescence and Gold Labeling. HeLa cells grown on slides or windows for XFM were serum starved for 1 h and treated with 10 nM NCs or NPs in serum-free EMEM for 1 h at 4 °C. This incubation allowed interaction between NCs and cell surface receptors, but at 4 °C endocytosis could not progress. Cells were washed with acidic glycine buffer to remove nonspecifically bound NCs or NPs. Afterward, samples were either incubated at 37 °C for 30 min or left at 4 °C. Subsequently, all slides or windows were washed with PBS, fixed in 4% formaldehyde in PEM buffer, and permeabilized in PEM with 0.2% Triton X-100 for immunolabeling. Rabbit monoclonal primary antibodies against EGFR (Epitomics) were used with goat anti-rabbit secondary antibodies conjugated to either AlexaFluor-488 (Abcam) for immunofluorescence or Fluoronanogold (Nanoprobes) for XFM. For immunofluorescence, cell nuclei were poststained with Hoechst 33342, while NPs and NCs were poststained with 1 mM ARS. Poststaining of NPs and NCs allows for maximal ARS coverage of the NP surface without interfering with ligand–receptor binding and is comparable to prelabeling of NPs with ARS for light microscopy.[49] ARS dye binds to the NP surface better than non-catechol carrying molecules adsorbed to the NP surface. Therefore, ARS outcompetes all NP surface interactions with the exception of DOPAC-functionalized peptides. It should be noted, however, that fluorescence quantum yield of alizarin reaches 0.001 at best,[93] 900-fold less than "standard" Alexa dyes (e.g., according to Invitrogen, fluorescence quantum yield for AlexaFluor-488 is 0.92). Therefore, in order to be visible after ARS staining, NC aggregates have to contain many particles.

Confocal fluorescence microscopy was performed on a Zeiss UV LSM 510 META (Carl Zeiss) with excitation/emission wavelengths of 405/420 nm for Hoechst, 488/505 nm for AlexaFluor-488, and 543/561 nm for ARS.

X-ray Fluorescence Microscopy. HeLa cells were grown on Si_3N_4 windows, treated with NCs, fixed with 4% formaldehyde, labeled with gold-conjugated antibodies, and air-dried in preparation for imaging at the X-ray microprobe at sector 2-ID-D at

the Advanced Photon Source at Argonne National Laboratory. The windows were raster scanned with 11.98 keV hard X-rays produced by an undulator source and monochromatized through a Kohzu Si<111> monochromator. The X-ray beam was focused by a Fresnel zone plate to a spot size of 200–250 nm. The cells were raster scanned with a step size of 500 nm and dwell time of 2 s per step (Figure 4a and b) or 200 nm and 2 s per step (Figure 4c and d). The X-ray-induced X-ray fluorescence at every scan step was recorded by an energy-dispersive silicon drift detector (Vortex EM, SII Nanotechnology). These data were against elemental NBS standards 1832 and 1833 using MAPS software in order to allow elemental quantification for each pixel.[94]

Cryogenic X-ray Fluorescence Microscopy and Tomography. For scanning at the Bionanoprobe, Si_3N_4 windows with NC-treated cells were washed and then plunge frozen in liquid ethane using a FEI Vitrobot (FEI). The samples were prescreened on a Nikon microscope equipped with an Instec CLM77K cryo-stage. These frozen-hydrated cells were then scanned at the Bionanoprobe at sector 21-ID-D with monochromatic 10 keV hard X-rays focused to a spot size of either 50 or 70 nm using Fresnel zone plates. The cells were raster scanned with a step size and dwell time of 200 nm and 400 ms (Figure 5a), 250 nm and 200 ms (Figure 5b and c), 150 nm and 500 ms (Figure 6a), 300 nm and 200 ms (Figure 6b and c), 200 nm and 400 ms (Figure 6d and e), and 250 nm and 200 ms (Figure 6f). The fluorescence spectra at each scan step were collected with a four-element silicon drift detector (Vortex ME-4, SII Nanotechnology) and fitted and quantified by comparison to a standard reference material (RF8-200-S2453, AXO Dresden GmbH) using MAPS software. Multiple angle projections of each cell were obtained (Supplementary Figures S8–S10, S12, and S13).

Tomographic Reconstruction of XFM Images. Twenty-three projections covering a total angular range of 138 degrees in six-degree increments were aligned *via* a cross-correlation algorithm and reconstructed *via* the ImageJ plugin TomoJ.[95] Algebraic reconstruction in TomoJ was performed with the simultaneous iterative reconstruction technique (SIRT) with 30 iterations and a relaxation coefficient of 1. The reconstructed Zn and Ti signals were visualized with Amira 5.4.5 (VSG/FEI).

Neutral Comet Assay. *Cell Preparation.* About 2.5×10^5 HeLa cells per dish were seeded and allowed to grow overnight. For comet assay experimental setups without inhibitors of EGFR nuclear transport, cells were serum starved for 1 h prior to NC treatment, then chilled to 4 °C for 30 min before the NCs were added directly to serum-free EMEM. The cells to be treated with EGFR nuclear translocation inhibitors (and cells exposed to mock inhibitor treatment) were seeded on T25 flasks and allowed to attach to the flask and grow for 12 h; at that time, cells were transferred to serum-free media. PBS or the small molecule inhibitor dasatinib (BioVision) was added to cell media to a final 10 μM treatment; this treatment lasted for 12 h prior to NC treatment as recommended in the literature.[52,72] Similarly, competitor peptide EGFR-NLS-phosphopetide AcRKRT(PO$_3$H$_3$)LRRLK[22,26] (synthesized by IBNAM Peptide Chemistry Core of Northwestern University) was added to cells in serum-free media 12 h prior to NC treatment; the final concentration of this peptide in media was 5 μM, as suggested in the literature.[22,26] NCs were added directly to each one of the plates, into serum-free EMEM to a final 10 nM concentration.

NC Treatments and Illuminations. For visible light illumination experiments (Figure 7a) cells were transferred to 4 °C 30 min prior to NC treatment, and the pairs of T25 flasks were then treated with PBS, 10 nM scrambled NCs, or 10 nM B-loop NCs for 30 min at 4 °C. One T25 flask from each treatment pair was then transferred to 37 °C and incubated for 1 h to allow for endocytosis and nuclear trafficking (samples labeled 60 min), while the other was kept at 4 °C (samples labeled 0 min). At the conclusion of the NC uptake period, cells were washed with PBS, scraped, and separated from each other by vigorous pipetting in a final volume of 800 μL of PBS. Half of the cells from each sample were resuspended in 400 μL of PBS and spread over the surface of a single well of a six-well plate and illuminated for 10 min. For this illumination a quartz halogen

lamp (Fiber Lite MI-150, Dolan Jenner) was used, producing primarily white light (with a transmittance of 20% at 400 nm). One T25 flask of cells was treated with 880 μM H$_2$O$_2$ for 20 min at 4 °C as a positive control.

T25 flasks with cells pretreated with EGFR nuclear translocation inhibitors were transferred to 4 °C 30 min prior to NC treatment, and the pairs of T25 flasks were then treated with PBS, 10 nM scrambled NCs, or 10 nM B-loop NCs for 30 min at 37 °C. UV illumination of NC-treated cells in the presence and absence of inhibitors of EGFR nuclear translocation was done similarly to that for white light. Cells from each sample were collected in PBS and split into two aliquots, and one was left in the dark while the other was illuminated with a UV lamp with 0.8 J/cm^2. Cells incubated for 20 min at room temperature with 25 μM potassium permanganate served as a control; under these conditions mild DNA damage (few DNA double-strand breaks) was to be expected.[96]

For short UV-light illumination (Supplementary Figures S14 and S15), prechilled cells in serum-free EMEM were treated with NCs for 30 min at 4 °C and then additionally incubated for 30 min at 37 °C. Half of the cells per treatment group were exposed to 0.3 J/cm^2 of UV light while suspended in 400 μL of PBS.

Cell Lysis and Comet Electrophoresis. Immediately upon illumination cells (in 400 μL of PBS) were mixed with 1.2 mL of 1% low melting point agarose with 2% DMSO, split in half and cast on two slides. Slides were submerged in neutral lysis solution (2% DMSO, 2% sarcosyl, 0.5 M Na$_2$EDTA, 0.5 mg/mL Proteinase K, pH = 8) and then lysed at 37 °C for 16–24 h. DMSO was added in order to prevent any possible additional DNA damage during the steps that followed. These slides, washed in running buffer (90 mM Tris, 90 mM boric acid, 2 mM Na$_2$EDTA, pH = 8.5) were subjected to electrophoresis at 0.6 V/cm for 25 min, all according to the published procedure for neutral comet assay.[67] DNA was stained for 30 min in 2.5 μg/mL propidium iodide and washed in water. Images of individual cells were collected either on a Tissue-Gnostics Cell Analysis microscope (TissueGnostics) or with a full field fluorescent Zeiss microscope using rhodamine filter.

Comet Data Analysis. The resulting images of individual cell comets were analyzed using CASP software (http://cas-plab.com/).[73] Olive tail moments for each sample are given in Supplementary Figure S14; total fluorescence and percent DNA in the tail comet parameters for each analyzed cell are presented in Supplementary Figure S15. Box whisker plots for cumulative percent tail DNA for each sample are shown in Figure 7. Plotting "percent tail DNA" for comet assay is considered the most suitable way to express the DNA damage when one wishes to compare effects of different DNA-damaging agents,[70] which is applicable to our case because we compared different DNA-damaging agents: NCs with H$_2$O$_2$ and KMnO$_4$.[71,96] Olive tail moment values, on the other hand, are used to show the extent of DNA damage when the same DNA-damaging agent is used.[67,68]

Overall Statistical Analysis. In all figures data points represent mean ± standard error unless otherwise noted. Differences in means were compared with Student's *t*-test with a significance level of 5%.

Conflict of Interest: The authors declare no competing financial interest.

REFERENCES AND NOTES

1. Guo, S.; Huang, L. Nanoparticles Escaping RES and Endosome: Challenges for siRNA Delivery for Cancer Therapy. *J. Nanomater.* **2011**, *2011*, 1–12.

2. Hillaireau, H.; Couvreur, P. Nanocarriers' Entry into the Cell: Relevance to Drug Delivery. *Cell. Mol. Life Sci.* **2009**, *66*, 2873–2896.

3. Fujishima, A.; Honda, K. Electrochemical Photolysis of Water at a Semiconductor Electrode. *Nature* **1972**, *238*, 37–38.

4. Paunesku, T.; Rajh, T.; Wiederrecht, G.; Maser, J.; Vogt, S.; Stojicevic, N.; Protic, M.; Lai, B.; Oryhon, J.; Thurnauer, M.; *et al.* Biology of TiO$_2$-Oligonucleotide Nanocomposites. *Nat. Mater.* **2003**, *2*, 343–346.

5. Tachikawa, T.; Majima, T. Single-Molecule Fluorescence Imaging of TiO$_2$ Photocatalytic Reactions. *Langmuir* **2009**, *25*, 7791–7802.

6. Salomon, D. S.; Brandt, R.; Ciardiello, F.; Normanno, N. Epidermal Growth Factor-Related Peptides and Their Receptors in Human Malignancies. *Crit. Rev. Oncol. Hematol.* **1995**, *19*, 183–232.

7. Henn, W.; Blin, N.; Zang, K. D. Polysomy of Chromosome 7 Is Correlated with Overexpression of the erbB Oncogene in Human Glioblastoma Cell Lines. *Hum. Genet.* **1986**, *74*, 104–106.

8. Tai, A. L. S.; Sham, J. S. T.; Xie, D.; Fang, Y.; Wu, Y.-L.; Hu, L.; Deng, W.; Tsao, G. S. W.; Qiao, G.-B.; Cheung, A. L. M.; *et al.* Co-Overexpression of Fibroblast Growth Factor 3 and Epidermal Growth Factor Receptor Is Correlated with the Development of Nonsmall Cell Lung Carcinoma. *Cancer* **2006**, *106*, 146–155.

9. Brand, T. M.; Iida, M.; Luthar, N.; Starr, M. M.; Huppert, E. J.; Wheeler, D. L. Nuclear EGFR as a Molecular Target in Cancer. *Radiother. Oncol.* **2013**, 1–8.

10. Gurtner, K.; Deuse, Y.; Bütof, R.; Schaal, K.; Eicheler, W.; Oertel, R.; Grenman, R.; Thames, H.; Yaromina, A.; Baumann, M.; *et al.* Diverse Effects of Combined Radiotherapy and EGFR Inhibition with Antibodies or TK Inhibitors on Local Tumour Control and Correlation with EGFR Gene Expression. *Radiother. Oncol.* **2011**, *99*, 323–330.

11. Kriegs, M.; Kasten-Pisula, U.; Rieckmann, T.; Holst, K.; Saker, J.; Dahm-Daphi, J.; Dikomey, E. The Epidermal Growth Factor Receptor Modulates DNA Double-Strand Break Repair by Regulating Non-Homologous End-Joining. *DNA Repair* **2010**, *9*, 889–897.

12. Psyrri, A.; Kassar, M.; Yu, Z.; Bamias, A.; Weinberger, P. M.; Markakis, S.; Kowalski, D.; Camp, R. L.; Rimm, D. L.; Dimopoulos, M. Effect of Epidermal Growth Factor Receptor Expression Level on Survival in Patients with Epithelial Ovarian Cancer. *Clin. Cancer Res.* **2005**, *11*, 8637–8643.

13. Psyrri, A.; Yu, Z.; Weinberger, P. M.; Sasaki, C.; Haffty, B.; Camp, R.; Rimm, D.; Burtness, B. A. Quantitative Determination of Nuclear and Cytoplasmic Epidermal Growth Factor Receptor Expression in Oropharyngeal Squamous Cell Cancer by Using Automated Quantitative Analysis. *Clin. Cancer Res.* **2005**, *11*, 5856–5862.

14. Marti, U.; Ruchti, C.; Kämpf, J.; Thomas, G. A.; Williams, E. D.; Peter, H. J.; Gerber, H.; Bürgi, U. Nuclear Localization of Epidermal Growth Factor and Epidermal Growth Factor Receptors in Human Thyroid Tissues. *Thyroid* **2001**, *11*, 137–145.

15. Rakowicz-Szulczynska, E. W. A. M.; Rodeck, U. Epidermal Growth Factor (EGF) and Monoclonal Antibody to Cell Surface EGF Receptor Bind to the Same Chromatin Receptor. *Arch. Biochem. Biophys.* **1989**, *268*, 456–464.

16. Rakowicz-Szulczynska, E. M.; Rodeck, U.; Herlyn, M.; Koprowski, H. Chromatin Binding of Epidermal Growth Factor, Nerve Growth Factor, and Platelet-Derived Growth Factor in Cells Bearing the Appropriate Surface Receptors. *Proc. Natl. Acad. Sci. U.S.A.* **1986**, *83*, 3728–3732.

17. Raper, S. E.; Burwen, S. J.; Barker, M. E.; Jones, A. L. Translocation of Epidermal Growth Factor to the Hepatocyte Nucleus during Rat Liver Regeneration. *Gastroenterology* **1987**, *92*, 1243–1250.

18. Campos, A. C. D. A.; Rodrigues, M. A.; de Andrade, C.; de Goes, A. M.; Nathanson, M. H.; Gomes, D. A. Epidermal Growth Factor Receptors Destined for the Nucleus Are Internalized via a Clathrin-Dependent Pathway. *Biochem. Biophys. Res. Commun.* **2011**, *412*, 1–11.

19. Kim, J.; Jahng, W. J.; Di Vizio, D.; Lee, J. S.; Jhaveri, R.; Rubin, M. A.; Shisheva, A.; Freeman, M. R. The Phosphoinositide Kinase PIKfyve Mediates Epidermal Growth Factor Receptor Trafficking to the Nucleus. *Cancer Res.* **2007**, *67*, 9229–9237.

20. Jaganathan, S.; Yue, P.; Paladino, D. C.; Bogdanovic, J.; Huo, Q.; Turkson, J. A Functional Nuclear Epidermal Growth Factor Receptor, SRC and Stat3 Heteromeric Complex in Pancreatic Cancer Cells. *PLoS One* **2011**, *6*, e19605.

21. Carpenter, G. Nuclear Localization and Possible Functions of Receptor Tyrosine Kinases. *Curr. Opin. Cell Biol.* **2003**, *15*, 143–148.

22. Dittmann, K.; Mayer, C.; Fehrenbacher, B.; Schaller, M.; Kehlbach, R.; Rodemann, H. P. Nuclear Epidermal Growth Factor Receptor Modulates Cellular Radio-Sensitivity by Regulation of Chromatin Access. *Radiother. Oncol.* **2011**, *99*, 317–322.

23. Lin, S. Y.; Makino, K.; Xia, W.; Matin, A.; Wen, Y.; Kwong, K. Y.; Bourguignon, L.; Hung, M. C. Nuclear Localization of EGF Receptor and Its Potential New Role as a Transcription Factor. *Nat. Cell Biol.* **2001**, *3*, 802–808.

24. Traynor, A. M.; Weigel, T. L.; Oettel, K. R.; Yang, D. T.; Zhang, C.; Kim, K.; Salgia, R.; Iida, M.; Brand, T. M.; Hoang, T.; *et al.* Nuclear EGFR Protein Expression Predicts Poor Survival in Early Stage Non-Small Cell Lung Cancer. *Lung Cancer* **2013**, *81*, 138–141.

25. Dittmann, K.; Mayer, C.; Fehrenbacher, B.; Schaller, M.; Raju, U.; Milas, L.; Chen, D. J.; Kehlbach, R.; Rodemann, H. P. Radiation-Induced Epidermal Growth Factor Receptor Nuclear Import Is Linked to Activation of DNA-Dependent Protein Kinase. *J. Biol. Chem.* **2005**, *280*, 31182–31189.

26. Dittmann, K.; Mayer, C.; Fehrenbacher, B.; Schaller, M.; Kehlbach, R.; Rodemann, H. P. Nuclear EGFR Shuttling Induced by Ionizing Radiation Is Regulated by Phosphorylation at Residue Thr654. *FEBS Lett.* **2010**, *584*, 3878–3884.

27. Yarden, Y.; Sliwkowski, M. X. Untangling the ErbB Signalling Network. *Nat. Rev. Mol. Cell Biol.* **2001**, *2*, 127–137.

28. Sorkin, A.; Goh, L. K. Endocytosis and Intracellular Trafficking of ErbBs. *Exp. Cell Res.* **2009**, *315*, 683–696.

29. Haglund, K.; Dikic, I. The Role of Ubiquitylation in Receptor Endocytosis and Endosomal Sorting. *J. Cell Sci.* **2012**, *125*, 265–275.

30. Lo, H.-W.; Hsu, S.-C.; Ali-Seyed, M.; Gunduz, M.; Xia, W.; Wei, Y.; Bartholomeusz, G.; Shih, J.-Y.; Hung, M.-C. Nuclear Interaction of EGFR and STAT3 in the Activation of the iNOS/NO Pathway. *Cancer Cell* **2005**, *7*, 575–589.

31. Hsu, S.-C.; Hung, M.-C. Characterization of a Novel Tripartite Nuclear Localization Sequence in the EGFR Family. *J. Biol. Chem.* **2007**, *282*, 10432–10440.

32. Lo, H.-W.; Ali-Seyed, M.; Wu, Y.; Bartholomeusz, G.; Hsu, S.-C.; Hung, M.-C. Nuclear-Cytoplasmic Transport of EGFR

Involves Receptor Endocytosis, Importin Beta1 and CRM1. *J. Cell. Biochem.* **2006**, *98*, 1570–1583.

33. Liao, H. J.; Carpenter, G. Role of the Sec61 Translocon in EGF Receptor Trafficking to the Nucleus and Gene Expression. *Mol. Biol. Cell* **2007**, *18*, 1064–1072.

34. de Jonge, M.; Holzner, C.; De Jonge, M. D.; Baines, S. B.; Twining, B. S.; Ignatyev, K.; Diaz, J.; Howard, D. L.; Legnini, D.; Miceli, A.; *et al*. Quantitative 3D Elemental Microtomography of Cyclotella Meneghiniana at 400-nm Resolution. *Proc. Natl. Acad. Sci. U.S.A.* **2010**, *107*, 15676–15680.

35. Arora, H. C.; Jensen, M. P.; Yuan, Y.; Wu, A.; Vogt, S.; Paunesku, T.; Woloschak, G. E. Nanocarriers Enhance Doxorubicin Uptake in Drug-Resistant Ovarian Cancer Cells. *Cancer Res.* **2012**, *72*, 769–778.

36. Bazak, R.; Ressl, J.; Raha, S.; Doty, C.; Liu, W.; Wanzer, B.; Salam, S. A.; Elwany, S.; Paunesku, T.; Woloschak, G. E. Cytotoxicity and DNA Cleavage with Core-Shell Nanocomposites Functionalized by a KH Domain DNA Binding Peptide. *Nanoscale* **2013**, *Jul 4*, 11394–11399.

37. Komoriya, A.; Hortsch, M.; Meyers, C.; Smith, M.; Kanety, H.; Schlessinger, J. Biologically Active Synthetic Fragments of Epidermal Growth Factor: Localization of a Major Receptor-Binding Region. *Proc. Natl. Acad. Sci. U.S.A.* **1984**, *81*, 1351–1355.

38. Lutsenko, S. V; Feldman, N. B.; Severin, S. E. Cytotoxic and Antitumor Activities of Doxorubicin Conjugates with the Epidermal Growth Factor and Its Receptor-Binding Fragment. *J. Drug Target* **2002**, *10*, 567–571.

39. Ohnishi, A.; Oda, Y.; Hayakawa, Y. Characterization of Receptors of Insect Cytokine, Growth-Blocking Peptide, in Human Keratinocyte and Insect Sf9 Cells. *J. Biol. Chem.* **2001**, *276*, 37974–37979.

40. Rabatic, B. M.; Dimitrijevic, N. M.; Cook, R. E.; Saponjic, Z. V; Rajh, T. Spatially Confined Corner Defects Induce Chemical Functionality of TiO_2 Nanorods. *Adv. Mater.* **2006**, *18*, 1033–1037.

41. Creutz, C.; Chou, M. H. Binding of Catechols to Mononuclear Titanium(IV) and to 1- and 5-nm TiO_2 Nanoparticles. *Inorg. Chem.* **2008**, *47*, 3509–3514.

42. Moser, J.; Punchihewa, S.; Infelta, P. P.; Graetzel, M. Surface Complexation of Colloidal Semiconductors Strongly Enhances Interfacial Electron-Transfer Rates. *Langmuir* **1991**, *7*, 3012–3018.

43. Xia, X.-R.; Monteiro-Riviere, N. A.; Riviere, J. E. An Index for Characterization of Nanomaterials in Biological Systems. *Nat. Nanotechnol.* **2010**, *5*, 671–675.

44. Sousa, S. R.; Moradas-Ferreira, P.; Saramago, B.; Melo, L. V.; Barbosa, M. A. Human Serum Albumin Adsorption on TiO_2 from Single Protein Solutions and from Plasma. *Langmuir* **2004**, *20*, 9745–9754.

45. Bayliss, R.; Littlewood, T.; Stewart, M. Structural Basis for the Interaction between FxFG Nucleoporin Repeats and Importin-Beta in Nuclear Trafficking. *Cell* **2000**, *102*, 99–108.

46. Wang, Y.-N.; Lee, H.-J. H.-H.; Du, Y.; Yamaguchi, H.; Hung, M.-C. Membrane-Bound Trafficking Regulates Nuclear Transport of Integral Epidermal Growth Factor Receptor (EGFR) and ErbB-2. *J. Biol. Chem.* **2012**, *287*, 16869–16879.

47. Gorlich, D.; Vogel, F.; Mills, A. D.; Hartmann, E.; Laskey, R. A. Distinct Functions for the Two Importin Subunits in Nuclear Protein Import. *Nature* **1995**, *377*, 246–248.

48. Thurn, K. T.; Arora, H.; Paunesku, T.; Wu, A.; Brown, E. M. B.; Doty, C.; Kremer, J.; Woloschak, G. Endocytosis of Titanium Dioxide Nanoparticles in Prostate Cancer PC-3M Cells. *Nanomedicine* **2010**, *1*, 1–8.

49. Thurn, K. T.; Paunesku, T.; Wu, A.; Brown, E. M. B.; Lai, B.; Vogt, S.; Maser, J.; Aslam, M.; Dravid, V.; Bergan, R.; *et al*. Labeling TiO_2 Nanoparticles with Dyes for Optical Fluorescence Microscopy and Determination of TiO_2-DNA Nanoconjugate Stability. *Small* **2009**, *5*, 1318–1325.

50. Giri, D. K.; Ali-seyed, M.; Li, L.; Lee, D.; Ling, P.; Bartholomeusz, G.; Wang, S.; Hung, M. Endosomal Transport of ErbB-2: Mechanism for Nuclear Entry of the Cell Surface Receptor. *Mol. Cell. Biol.* **2005**, *25*, 11005–11018.

51. Lo, H.-W.; Xia, W.; Wei, Y.; Ali-Seyed, M.; Huang, S.-F.; Hung, M.-C. Novel Prognostic Value of Nuclear Epidermal Growth Factor Receptor in Breast Cancer. *Cancer Res.* **2005**, *65*, 338–348.

52. Li, C.; Iida, M.; Dunn, E. F.; Ghia, A. J.; Wheeler, D. L. Nuclear EGFR Contributes to Acquired Resistance to Cetuximab. *Oncogene* **2009**, *28*, 3801–3813.

53. Xia, W.; Wei, Y.; Du, Y.; Liu, J.; Chang, B.; Yu, Y.-L.; Huo, L.-F.; Miller, S.; Hung, M.-C. Nuclear Expression of Epidermal Growth Factor Receptor Is a Novel Prognostic Value in Patients with Ovarian Cancer. *Mol. Carcinog.* **2009**, *48*, 610–617.

54. Xu, Y.; Shao, Y.; Zhou, J.; Voorhees, J. J.; Fisher, G. J. Ultraviolet Irradiation-Induces Epidermal Growth Factor Receptor (EGFR) Nuclear Translocation in Human Keratinocytes. *J. Cell. Biochem.* **2009**, *107*, 873–880.

55. Paunesku, T.; Vogt, S.; Lai, B.; Maser, J.; Stojicevic, N.; Thurn, K. T.; Osipo, C.; Liu, H.; Legnini, D.; Wang, Z.; *et al*. Intracellular Distribution of TiO_2-DNA Oligonucleotide Nanoconjugates Directed to Nucleolus and Mitochondria Indicates Sequence Specificity. *Nano Lett.* **2007**, *7*, 596–601.

56. Ralle, M.; Lutsenko, S. Quantitative Imaging of Metals in Tissues. *Biometals* **2009**, *22*, 197–205.

57. Finney, L.; Mandava, S.; Ursos, L.; Zhang, W.; Rodi, D.; Vogt, S.; Legnini, D.; Maser, J.; Ikpatt, F.; Olopade, O. I.; *et al*. X-Ray Fluorescence Microscopy Reveals Large-Scale Relocalization and Extracellular Translocation of Cellular Copper during Angiogenesis. *Proc. Natl. Acad. Sci. U.S.A.* **2007**, *104*, 2247–2252.

58. McRae, R.; Lai, B.; Fahrni, C. J. Copper Redistribution in Atox1-Deficient Mouse Fibroblast Cells. *J. Biol. Inorg. Chem.* **2010**, *15*, 99–105.

59. Ortega, R.; Bohic, S.; Tucoulou, R.; Somogyi, A.; Devès, G. Microchemical Element Imaging of Yeast and Human Cells Using Synchrotron X-Ray Microprobe with Kirkpatrick-Baez Optics. *Anal. Chem.* **2004**, *76*, 309–314.

60. McRae, R.; Lai, B.; Vogt, S.; Fahrni, C. J. Correlative microXRF and Optical Immunofluorescence Microscopy of Adherent Cells Labeled with Ultrasmall Gold Particles. *J. Struct. Biol.* **2006**, *155*, 22–29.

61. Steinbrecht, R. A.; Zierold, K. *Cryotechniques in Biological Electron Microscopy*; Springer-Verlag: Berlin, 1987.

62. Cai, R. X.; Kubota, Y.; Shuin, T.; Sakai, H.; Hashimoto, K.; Fujishima, A. Induction of Cytotoxicity by Photoexcited TiO_2 Particles. *Cancer Res.* **1992**, *52*, 2346–2348.

63. George, S.; Pokhrel, S.; Ji, Z.; Henderson, B. L.; Xia, T.; Li, L.; Zink, J. I.; Nel, A. E.; Mädler, L. Role of Fe Doping in Tuning the Band Gap of TiO_2 for the Photo-Oxidation-Induced Cytotoxicity Paradigm. *J. Am. Chem. Soc.* **2011**, *133*, 11270–11278.

64. He, Q.; Zhang, Z.; Xiong, J.; Xiong, Y.; Xiao, H. A Novel Biomaterial—Fe_3O_4:TiO_2 Core-Shell Nano Particle with Magnetic Performance and High Visible Light Photocatalytic Activity. *Opt. Mater.* **2008**, *31*, 380–384.

65. Serpone, N.; Salinaro, A.; Horikoshi, S.; Hidaka, H. Beneficial Effects of Photo-Inactive Titanium Dioxide Specimens on Plasmid DNA, Human Cells and Yeast Cells Exposed to UVA/UVB Simulated Sunlight. *J. Photochem. Photobiol., A* **2006**, *179*, 200–212.

66. Roots, R.; Okada, S. Estimation of Life Times and Diffusion Distances of Radicals Involved in X-Ray-Induced DNA Strand Breaks or Killing of Mammalian Cells. *Radiat. Res.* **1975**, *64*, 306–320.

67. Olive, P. L.; Banáth, J. P. The Comet Assay: A Method to Measure DNA Damage in Individual Cells. *Nat. Protoc.* **2006**, *1*, 23–29.

68. Olive, P. L. Impact of the Comet Assay in Radiobiology. *Mutat. Res.* **2009**, *681*, 13–23.

69. Testard, I.; Sabatier, L. Assessment of DNA Damage Induced by High-LET Ions in Human Lymphocytes Using the Comet Assay. *Mutat. Res.* **2000**, *448*, 105–115.

70. Grigaravicius, P.; Rapp, A.; Greulich, K. O. A Direct View by Immunofluorescent Comet Assay (IFCA) of DNA Damage Induced by Nicking and Cutting Enzymes, Ionizing (137)Cs

Radiation, UV-A Laser Microbeam Irradiation and the Radiomimetic Drug Bleomycin. *Mutagenesis* **2009**, *24*, 191–197.

71. Collins, A. R. The Comet Assay for DNA Damage and Repair. *Mol. Biotechnol.* **2004**, *26*, 249–261.

72. Raju, U.; Riesterer, O.; Wang, Z.-Q.; Molkentine, D. P.; Molkentine, J. M.; Johnson, F. M.; Glisson, B.; Milas, L.; Ang, K. K. Dasatinib, a Multi-Kinase Inhibitor Increased Radiation Sensitivity by Interfering with Nuclear Localization of Epidermal Growth Factor Receptor and by Blocking DNA Repair Pathways. *Radiother. Oncol. J. Eur. Soc. Ther. Radiol. Oncol.* **2012**, *105*, 241–249.

73. Garcia, O.; Romero, I.; González, J. E.; Mandina, T. Measurements of DNA Damage on Silver Stained Comets Using Free Internet Software. *Mutat. Res.* **2007**, *627*, 186–190.

74. Yu, H.; Nie, Y.; Dohmen, C.; Li, Y.; Wagner, E. Epidermal Growth Factor-PEG Functionalized PAMAM-Pentaethylenehexamine Dendron for Targeted Gene Delivery Produced by Click Chemistry. *Biomacromolecules* **2011**, *12*, 2039–2047.

75. Zeng, F.; Lee, H.; Allen, C. Epidermal Growth Factor-Conjugated Poly(ethylene glycol)-Block-Poly(delta-valerolactone) Copolymer Micelles for Targeted Delivery of Chemotherapeutics. *Bioconjugate Chem.* **2006**, *17*, 399–409.

76. Li, Z.; Zhao, R.; Wu, X.; Sun, Y.; Yao, M.; Li, J.; Xu, Y.; Gu, J. Identification and Characterization of a Novel Peptide Ligand of Epidermal Growth Factor Receptor for Targeted Delivery of Therapeutics. *FASEB J.* **2005**, *19*, 1978–1985.

77. Yang, L.; Mao, H.; Wang, Y. A.; Cao, Z.; Peng, X.; Wang, X.; Duan, H.; Ni, C.; Yuan, Q.; Adams, G.; *et al.* Single Chain Epidermal Growth Factor Receptor Antibody Conjugated Nanoparticles for *in Vivo* Tumor Targeting and Imaging. *Small* **2009**, *5*, 235–243.

78. Raha, S.; Paunesku, T.; Woloschak, G. Peptide-Mediated Cancer Targeting of Nanoconjugates. *Wiley Interdiscip. Rev. Nanomed. Nanobiotechnol.* **2011**, *3*, 269–281.

79. Paulo, C. S. O.; Pires das Neves, R.; Ferreira, L. S. Nanoparticles for Intracellular-Targeted Drug Delivery. *Nanotechnology* **2011**, *22*, 494002.

80. Han, W.; Lo, H.-W. Landscape of EGFR Signaling Network in Human Cancers: Biology and Therapeutic Response in Relation to Receptor Subcellular Locations. *Cancer Lett.* **2012**, *318*, 124–134.

81. Beetz, T.; Jacobsen, C. Soft X-Ray Radiation-Damage Studies in PMMA Using a Cryo-STXM. *J. Synchrotron Radiat.* **2003**, *10*, 280–283.

82. Pommier, Y.; Topoisomerase, I. Inhibitors: Camptothecins and Beyond. *Nat. Rev. Cancer* **2006**, *6*, 789–802.

83. Rajendran, L.; Knölker, H.-J.; Simons, K. Subcellular Targeting Strategies for Drug Design and Delivery. *Nat. Rev. Drug Discovery* **2010**, *9*, 29–42.

84. Romanello, M. B.; Fidalgo de Cortalezzi, M. M. An Experimental Study on the Aggregation of TiO_2 Nanoparticles under Environmentally Relevant Conditions. *Water Res.* **2013**, *47*, 3887–3898.

85. Monopoli, M. P.; Åberg, C.; Salvati, A.; Dawson, K. A. Biomolecular Coronas Provide the Biological Identity of Nanosized Materials. *Nat. Nanotechnol.* **2012**, *7*, 779–786.

86. Dutta, D.; Sundaram, S. K.; Teeguarden, J. G.; Riley, B. J.; Fifield, L. S.; Jacobs, J. M.; Addleman, S. R.; Kaysen, G. A.; Moudgil, B. M.; Weber, T. J. Adsorbed Proteins Influence the Biological Activity and Molecular Targeting of Nanomaterials. *Toxicol. Sci.* **2007**, *100*, 303–315.

87. Mano, S. S.; Kanehira, K.; Sonezaki, S.; Taniguchi, A. Effect of Polyethylene Glycol Modification of TiO_2 Nanoparticles on Cytotoxicity and Gene Expressions in Human Cell Lines. *Int. J. Mol. Sci.* **2012**, *13*, 3703–3717.

88. Deng, Z. J.; Mortimer, G.; Schiller, T.; Musumeci, A.; Martin, D.; Minchin, R. F. Differential Plasma Protein Binding to Metal Oxide Nanoparticles. *Nanotechnology* **2009**, *20*, 455101.

89. Cho, E.; Zhang, Q.; Xia, Y. The Effect of Sedimentation and Diffusion on Cellular Uptake of Gold Nanoparticles. *Nat. Nanotechnol.* **2011**, *6*, 385–391.

90. Krumpfer, J. W.; Schuster, T.; Klapper, M.; Müllen, K. Make It Nano-Keep It Nano. *Nano Today* **2013**, *8*, 417–438.

91. Zhu, M.; Perrett, S.; Nie, G. Understanding the Particokinetics of Engineered Nanomaterials for Safe and Effective Therapeutic Applications. *Small* **2013**, *9*, 1619–1634.

92. Otsuka, H.; Nagasaki, Y.; Kataoka, K. PEGylated Nanoparticles for Biological and Pharmaceutical Applications. *Adv. Drug Delivery Rev.* **2003**, *55*, 403–419.

93. Zhang, L.; Dong, S.; Zhu, L. Fluorescent Dyes of the Esculetin and Alizarin Families Respond to Zinc Ions Ratiometrically. *Chem. Commun. (London)* **2007**, 1891–1893.

94. Vogt, S.; Maser, J.; Jacobsen, C. Data Analysis for X-Ray Fluorescence Imaging. *J. Phys. IV* **2003**, *104*, 617–622.

95. Messaoudii, C.; Boudier, T.; Sanchez Sorzano, C. O.; Marco, S. TomoJ: Tomography Software for Three-Dimensional Reconstruction in Transmission Electron Microscopy. *BMC Bioinf.* **2007**, *8*, 288.

96. Soni, B.; Visavadiya, N. P.; Dalwadi, N.; Madamwar, D.; Winder, C.; Khalil, C. Purified C-Phycoerythrin: Safety Studies in Rats and Protective Role against Permanganate-Mediated Fibroblast-DNA Damage. *J. Appl. Toxicol.* **2010**, *30*, 542–550.